

# Lithospheric Structure of the Arabian Shield from Joint Inversion of P- and S-Wave Receiver Functions and Dispersion Velocities

Abdullah M. Al-Amri

Dept. of Geology & Geophysics, King Saud Univ. Riyadh, Saudi Arabia  
E. mail: [amsamri@ksu.edu.sa](mailto:amsamri@ksu.edu.sa), Tel: 00966114676198; Fax: 00966114673662

## Abstract

New velocity models of lithospheric thickness and velocity structure have been developed for the Arabian Shield by three tasks: 1) Computing P-Wave Receiver Functions (PRFs) and S-Wave Receiver Functions (SRFs) for all the broadband stations within the Saudi seismic networks. The number of receiver function waveforms depends on the recording time window and quality of the broadband station. 2) Computing ambient noise correlation Green's functions for all available station pairs within the Saudi seismic networks to image the shear velocity in the crust and uppermost mantle beneath the Arabian Peninsula. Together they provided hundreds of additional, unique paths exclusively sampling the region of interest. Both phase and group velocities for all the resulting empirical Green's functions have been measured and to be used in the joint inversion. 3) Jointly inverted the PRFs and SRFs obtained in task 1 with dispersion velocities measured on the Green's functions obtained in task 2 and with fundamental-mode, Rayleigh-wave, group and phase velocities borrowed from the tomographic studies to precisely determine 1D crustal velocity structure and upper mantle. The analysis of the PRFs revealed values of 25 - 45 km for crustal thickness, with the thin crust next to the Red Sea and Gulf of Aqaba and the thicker crust under the platform, and  $V_p/V_s$  ratios in the 1.70 – 1.80 range, suggesting a range of compositions (felsic to mafic) for the shield's crust. The migrated SRFs suggest lithospheric thicknesses in the 80-100 km range for portions of the shield close to the Red Sea and Gulf of Aqaba and near the Arabian Gulf. Generally, the novelty of the velocity models developed under this paper has consisted in the addition of SRF data to extend the velocity models down to lithospheric and sub-lithospheric depths.

**Keywords:** Receiver function, Crustal structure, Arabian shield, ambient noise, seismic velocities, lithospheric thickness.

## 1. Introduction

The Arabian Shield comprises about one-third of the western Arabian Peninsula and is mostly composed of Precambrian metamorphic and plutonic rocks. It is clear example of late Precambrian plate tectonics, crustal growth, and a superb example of a recently rifted continent that follows the ideas of plate tectonics. Moreover, although the shield is composed of Precambrian terrains, it contains Tertiary and Quaternary volcanic rocks - the *harrats* - that related to the early stages of the Red Sea formation and possibly to plume-related lithospheric erosion (Stoesser and Camp, 1985; Camp and Roobol, 1992). Mapping the subsurface structure of the Shield is therefore an important step towards improving our understanding of the continental growth processes and subsequent modifications through rifting and plume-lithosphere interaction.

Current models of Precambrian crustal evolution (Durrheim and Mooney, 1991) predict that Proterozoic terranes are underlain by fertile (FeO-rich) cratonic roots that will allow the production of mafic magmas and the under plating of the Proterozoic crust upon heating by a thermal event. Interestingly, seismic velocity models of the crust and uppermost mantle of the shield revealed crustal thicknesses under 40 km and lower crustal velocities below 4.0 km/s, suggesting the absence of a layer of mafic under plate under the Arabian terrains. Nevertheless, the surface volcanism points towards recent (<30 Ma) generation of magmas in the continental lithosphere. Therefore, imaging of the continental lithosphere under the Arabian Shield might provide a unique opportunity for imaging the initial stages of mafic crustal under plating postulated by Durrheim and Mooney (1991).

In this paper, new velocity models of lithospheric thickness and velocity structure for the Arabian Shield by jointly inverting multiple data sets have been tried: P-wave receiver functions, S-wave receiver functions, surface-wave dispersion velocities, and ambient-noise cross-correlation dispersion velocities. These velocity models can provide robustly constrained images of the velocity structure of the Arabian lithosphere and determine the depth of seismic discontinuities bounding the top and bottom of Lower Velocity Zones (LVZs) associated with the migration of magma within the crust and lithospheric mantle. The velocity models that will be produced through the joint inversion of multiple datasets will be better constrained and have better resolution than other known models for the region. This is because we will try to fit four complimentary seismic datasets in our inversions. The joint inversion will take advantage of P-wave receiver functions to constrain depths to intra-crustal discontinuities and crustal thickness, S-wave receiver functions to constrain depths to lithospheric discontinuities and lithospheric thickness, and the dispersion velocities from ambient noise cross-correlation and surface-waves to constrain velocities and velocity gradients in the shallow crust and continental lithosphere.

The resolution of the velocity-depth profiles obtained by the joint inversion of receiver functions and dispersion velocities is a combination of the resolving power of the data sets. Our experience suggests that S-wave velocities and layer thicknesses are generally constrained within 0.1 km/s and 2.5 km in the crust and uppermost mantle, and that the resolution degrades with depth (Juliá et al. 2003; Juliá et al. 2008; Juliá et al. 2009). Laterally, the resolution is at best within the size of one surface-wave tomographic cell (typically  $1^{\circ} \times 1^{\circ}$ ). Teleseismic P-waveforms recorded at three-component seismic stations contain much information on the earthquake source, the structure near both the source and the receiver, and the mantle path in between. PRFs are obtained by removing the effects of the source and the path to isolate near-receiver structure (Langston, 1979). At relatively sharp velocity discontinuities, several percent of an incoming P-wave's energy is converted to an S-wave; the amplitudes of the resulting P-to-S conversions carry important information on the velocity contrast across the discontinuity and the S-P travel-times of the conversions depend on the depth of the discontinuity as well as the velocity of the structure above it. Examining both the radial and tangential receiver functions can provide additional constraints on dipping interfaces and anisotropy (Cassidy, 1992; Levin and Park, 1997).

The joint inversion of P-wave receiver functions (PRFs) and surface-wave dispersion velocities has proven an effective tool for determining the 1D velocity structure of the continental crust and its underlying uppermost mantle (Juliá et al. 2008; Juliá et al. 2009; Juliá et al. 2005; Dugda et al. 2007; Keranen et al. 2009; Kgaswane et al. 2009). Both PRFs and surface-wave dispersion are mostly sensitive to S-wave velocity, but the constraints conveyed

by each data set are different. PRFs are mostly sensitive to subsurface seismic discontinuities, constraining S-P travel-times between the discontinuities and the free surface and the S-wave velocity contrasts across them.

To date, most ambient seismic noise research has focused on group velocity measurements of the resulting surface waves (Moschetti et al. 2007; Shairo et al. 2005) although more recently, work has begun on measuring the phase velocities (Lin et al. 2008) and amplitudes (Prieto and Beroza, 2008; Matzel, 2008) and the new discoveries and methodologies are constantly being developed.

## 2. Seismotectonic Setting

Figure (1) shows a map of the Arabian Peninsula along with major tectonic features and earthquake occurrences. Active tectonics of the region is dominated by the collision of the Arabian Plate with the Eurasian Plate along the Zagros and Bitlis Thrust systems, rifting and seafloor spreading in the Red Sea and Gulf of Aden. Strike-slip faulting occurs along the Gulf of Aqabah and Dead Sea Transform fault systems. The framework of the shield is composed of Precambrian rocks and metamorphosed sedimentary and intruded by granites. The fold-fault pattern of the shield, together with some stratigraphic relationships suggests that the shield have undergone two orogenic cycles. To the first order, the Arabian shield is composed of two layers, each about 20km thick, with average velocities of about 6.3 km/s and 7 km/s respectively (Mooney et al. 1985). The crust thins rapidly to less than 20 km at the western shield margin, beyond which the sediments of the Red Sea shelf and coastal plain are underlain by oceanic crust.

The crustal thickness in the Arabian Shield varies from about 15 km in the Red Sea, to 20 km along the Red Sea coast to about 35-40 km in the in central Arabian Shield (Al-Amri, 1998; Al-Damegh et al. 2005; Tkacic et al. 2006). Reports of large-scale seismic tomography (Debayle et al. 2001) suggest that a low-velocity anomaly in the upper mantle extends laterally beneath the Arabian Shield from the Red Sea in the west to the Shield-Platform boundary in the east. It is known that high-frequency regional phase behavior in the Arabian Plate is quite variable as demonstrated by Al-Damegh et al. (2005). They investigated the attenuation of  $P_n$  phase ( $Q_{P_n}$ ) for 1–2 Hz along the Red Sea, the Dead Sea fault system, within the Arabian Shield and in the Arabian Platform. Consistent with the  $S_n$  attenuation, they observed low  $Q_{P_n}$  values of 22 and 15 along the western coast of the Arabian Plate and along the Dead Sea fault system, respectively, for a frequency of 1.5 Hz. Higher  $Q_{P_n}$  values of the order of 400 were observed within the Arabian Shield and Platform for the same frequency. Their results based on  $S_n$  and  $P_n$  observations along the western and northern portions of the Arabian Plate imply the presence of an anomalously hot and thinned lithosphere in these regions that may be caused by the extensive upper mantle anomaly that appears to span most of East Africa and western Arabia.

Pasyanos et al. (2009b) applied a technique to simultaneously invert amplitudes measurements of  $P_n$ ,  $P_g$ ,  $S_n$  and  $L_g$  to produce P-wave and S-wave attenuation models of the crust and upper mantle. Their attenuation is modeled as P-wave and S-wave attenuation surfaces for the crust, and similar set for the upper mantle. They used all of the phase amplitudes together by using different (source, geometrical-spreading, site, and attenuation) terms for each phase.

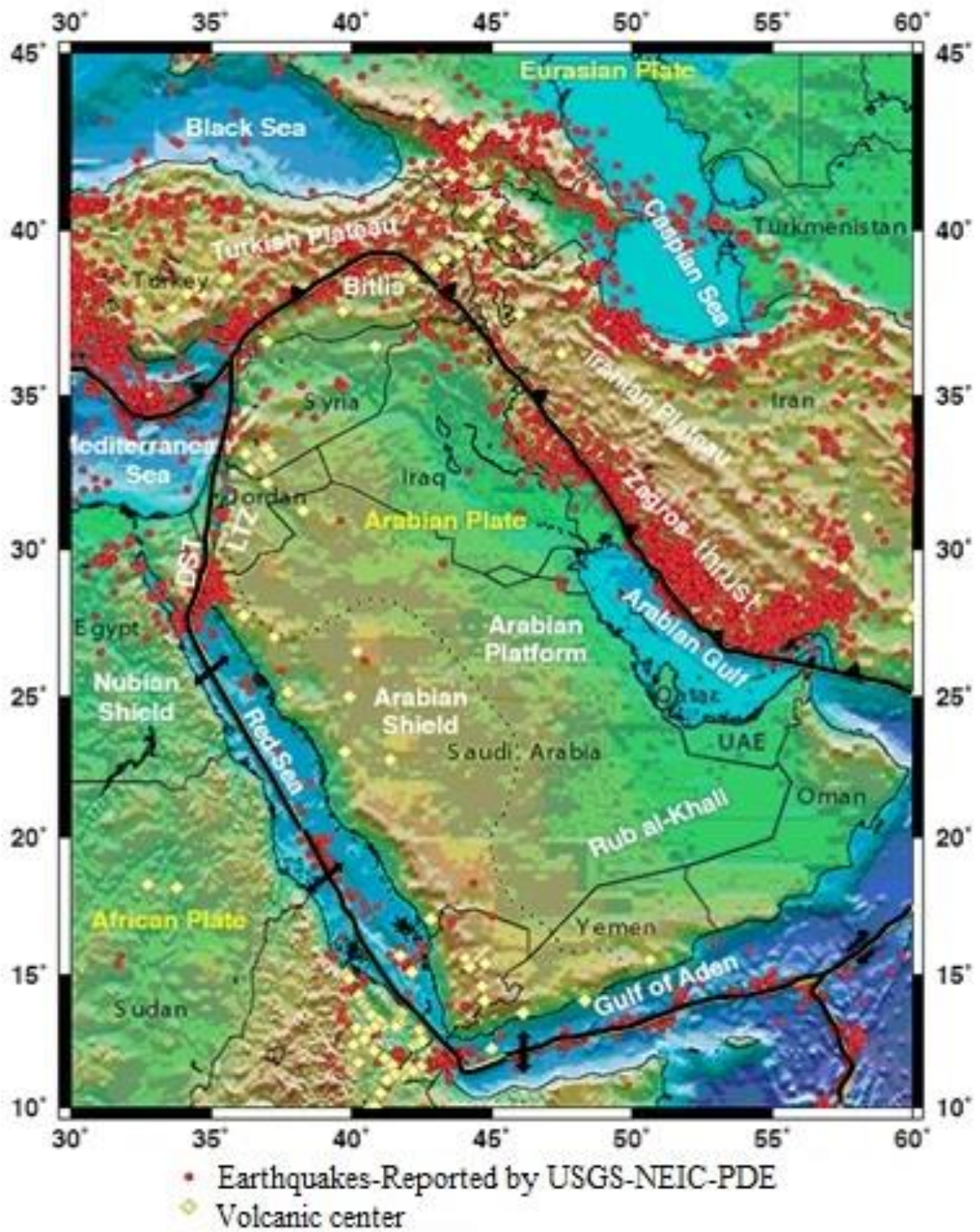


Fig. 1. Seismotectonic map of the Arabian Peninsula and Arabian plate boundaries showing earthquake locations and volcanic centers.

### 3. Analytical Methods

#### 3.1 Computation of P-wave receiver functions

PRFs and SRFs have been computed for all the broadband stations within the Saudi seismic networks. We followed the approaches of Langston (1979) and Sodoudi (2005) for the computation of PRFs and SRFs, respectively, along with the iterative deconvolution method of Ligorria and Ammon (1999). The number of receiver function waveforms depended on the recording time window and quality of the broadband station. The data set for the computation of PRFs consisted of teleseismic P-waveforms for seismic sources located between 30° and 90° epicentral distance and with magnitude 5.5  $m_b$  or larger recorded at broadband seismic stations in Saudi Arabia (Fig. 2).

The selected waveforms were processed to obtain P-wave receiver function estimates for all the stations (Langston (1979)). First, the waveforms were windowed 10 s before and 110 s after the teleseismic P-wave arrival, detrended, and tapered with a cosine taper function of 5% width. The waveforms were then high-pass filtered with a 3-pole Butterworth filter at 20 s to remove long-period noise, and decimated to 10 samples per second after low-pass filtering below 8 Hz to avoid aliasing. The filtered waveforms were rotated into the ZRT cylindrical- coordinate system and the vertical component (Z) was then deconvolved from the radial (R) and transverse (T) components to produce radial and transverse receiver functions, respectively, for each event. The deconvolution was implemented through the iterative time-domain procedure of Ligorria and Ammon (1999) with 500 iterations, at two overlapping Gaussian widths of 2.5 ( $f_c \leq 1.25$  Hz) and 1.0 ( $f_c \leq 0.5$  Hz) to remove high-frequency noise.

From the deconvolved waveforms we selected high-quality receiver functions for our analysis. First, the performance of the deconvolution process was assessed by computing the root-mean-square (RMS) misfit between the original radial waveform and the recovered radial waveform obtained after convolving the receiver function back with the vertical component. Receiver functions with percent recoveries under 85% were rejected. Second, transverse receiver functions were examined and the corresponding radial receiver functions were rejected if significant signal was observed. This step ensured that radial receiver functions were not significantly disrupted by small-scale lateral heterogeneities under the recording station. Finally, the remaining radial receiver functions were overlapped to visually identify outliers, which were removed from the data set. The final number of selected PRFs for each station and frequency band is reported in Table 1.

#### 3.2 Crustal thickness and bulk Vp/Vs ratios

The hk-stacking technique of Zhu and Kanamori (2000) has been applied PRFs with frequencies ( $f_c \leq 1.25$  Hz) to obtain thickness and bulk Vp/Vs ratios for the crust under each recording station in Saudi Arabia. The technique consists of a transformation from a time-domain representation of the PRFs into a new domain, which is a function of the depth to the interface (H) and Vp/Vs (k) ratio. The transformation is described as;

$$s(H, k) = \sum [w_1 r f_i(t_1) + w_2 r f_i(t_2) - w_3 r f_i(t_3)], \quad (3.2.1)$$

where  $r f_i(t_j)$  are the receiver function amplitudes at  $t=t_j$ ,  $w_i$  are *a priori* weights such that  $\sum w_i = 1$ , and the summation extends to all the PRFs for a given station. The times  $t_j$  are given by

$$t_1 = t_{Ps} - t_P = H (\pi\beta - \pi\alpha) \quad (3.2.2a)$$

$$t_2 = t_{pPs} - t_p = H (\pi_\beta + \pi_\alpha) \quad (3.2.2b)$$

$$t_3 = t_{PsPs} - t_p = 2H \pi_\beta, \quad (3.2.2c)$$

where  $\pi$  is the vertical slowness (obtained through a trial  $k$  value and an a priori value for crustal P-wave velocity) and  $H$  is a trial depth. During the transformation, the amplitudes of P-to-S conversions at the computed times  $t_j$  will interact constructively only when the trial  $H$  and  $V_p/V_s$  ratios coincide with the depth to and  $V_p/V_s$  ratio above an actual discontinuity. The results on crustal thickness and  $V_p/V_s$  ratio for the broadband stations in Saudi Arabia are displayed in Fig.(3) and listed in Table (2), along with  $2\sigma$  confidence bounds obtained after bootstrapping the original dataset with 200 replications (Efron and Tibshirai, 1991) and other relevant information.

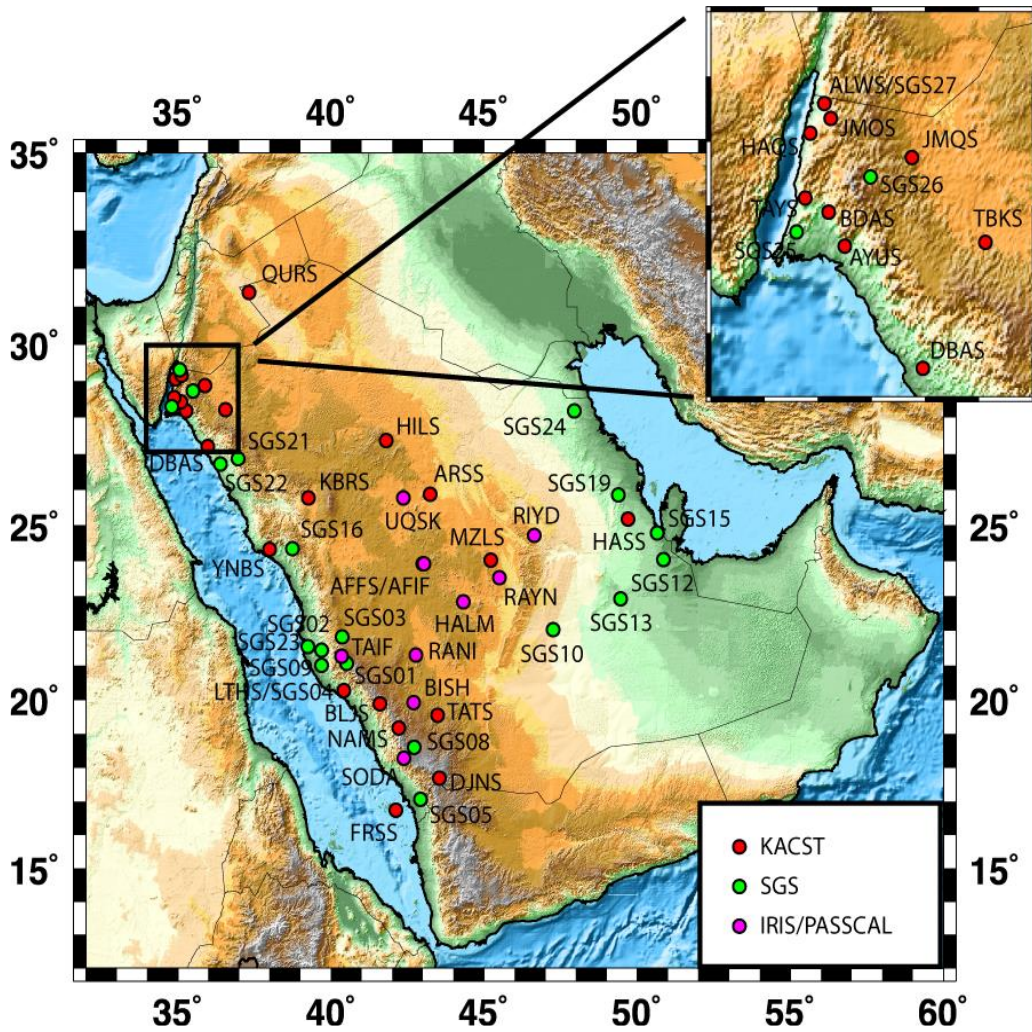


**Fig. 2.** Topographic map of the Arabian Peninsula showing the broadband stations. The stations belong to three different networks: King Saud Center for Science and Technology (KACST), Saudi Geological Survey (SGS), and the Incorporated Research Institutes for Seismology (IRIS).

**Table 1** Stations and waveform statistics for the selected dataset.

Station name	Latitude (deg)	Longitude (deg)	Start Time (year.jday)	End Time (year.jday)	P-wave	PRFs (a=2.5)	PRFs (a=1.0)	S-wave	SRFs (a=1.0)
<b>KACST Network</b>									
affs	23.927	43.001	2000.125	2006.300	1350	88	62	177	9
alws	29.310	35.065	1999.312	2006.029	1533	84	94	188	9
arss	25.881	43.237	2001.145	2005.360	186	22	18	19	3
ayus	28.189	35.269	2000.133	2006.296	1170	68	56	159	6
bdas	28.432	35.101	1999.312	2006.296	1407	67	61	179	6
bljs	19.881	41.599	2000.241	2006.300	1689	104	90	153	6
djns	17.707	43.543	2001.021	2006.300	1449	86	89	157	5
frss	16.739	42.114	2002.062	2006.300	828	34	49	85	1
haqs	29.055	34.930	1999.312	2006.296	1470	83	71	181	7
hass	25.190	49.694	2000.088	2006.300	1440	93	78	305	20
hils	27.384	41.792	2000.088	2006.300	1638	139	116	234	14
jmos	29.169	35.109	2000.156	2006.296	1437	71	75	178	4
jmqs	28.886	35.878	2002.064	2006.296	762	41	35	102	2
kbrs	25.789	39.262	2000.202	2005.175	177	25	23	7	1
lths	20.275	40.411	2000.241	2006.120	807	34	35	49	5
mzls	24.028	45.207	2004.007	2006.300	1305	87	63	208	4
nams	19.171	42.208	1999.312	2006.300	735	62	54	86	4
qurs	31.386	37.324	2000.125	2006.292	1182	58	55	179	5
tats	19.541	43.478	2000.156	2006.300	1245	79	73	148	6
tays	28.551	34.872	2000.125	2006.296	651	37	35	85	3
tbks	28.225	36.549	1999.312	2006.296	1641	93	81	181	5
ynbs	24.340	37.992	1999.312	2006.296	1146	64	55	116	5
<b>IRIS-PASSCAL Network</b>									
afif	23.931	43.040	1995.328	1997.052	363	53	34	48	6
halm	22.845	44.317	1995.328	1997.052	543	74	64	25	5
rani	21.312	42.776	1995.344	1997.057	333	30	20	20	10
rayn	23.522	45.501	1995.337	2008.354	3870	456	335	164	37
riyd	24.722	46.643	1996.076	1997.059	438	33	28	36	8
soda	18.292	42.377	1995.344	1997.057	516	55	42	11	0
taif	21.281	40.349	1996.158	1996.240	90	11	10	4	1
uqsk	25.789	42.360	1996.163	1997.052	387	31	22	16	1
<b>SGS Network</b>									
sgs01	21.058	40.518	2006.259	2007.216	168	30	28	17	1
sgs02	21.449	39.691	2006.259	2007.216	183	31	28	16	1
sgs03	21.834	40.359	2006.321	2007.216	153	27	25	16	1
sgs04	20.276	40.411	2006.359	2007.216	144	25	22	15	1
sgs05	17.068	42.917	2006.359	2007.216	123	22	24	13	2
sgs08	18.606	42.719	2007.125	2007.216	69	12	9	39	0
sgs09	21.005	39.683	2006.109	2007.076	138	26	21	14	4
sgs10	22.039	47.245	2006.109	2007.216	117	22	17	15	3
sgs12	24.046	50.846	2006.109	2007.216	246	46	44	41	8
sgs13	22.927	49.462	2006.109	2007.216	234	43	36	39	9
sgs15	24.798	50.644	2006.109	2007.216	240	40	36	40	7
sgs16	24.358	38.743	2006.109	2007.216	231	43	43	23	2
sgs19	25.869	49.376	2006.109	2007.216	246	42	38	42	9
sgs21	26.867	36.958	2007.197	2007.216	33	7	5	2	0
sgs22	26.732	36.393	2006.109	2007.216	225	43	36	23	3
sgs23	21.557	39.236	2006.109	2007.216	246	50	42	39	7
sgs24	28.187	47.942	2006.109	2007.216	255	59	48	43	9
sgs25	28.300	34.797	2006.109	2007.216	222	29	26	28	1
sgs26	28.735	35.492	2006.109	2007.216	243	50	41	31	4
sgs27	29.300	35.062	2006.109	2007.216	246	48	45	31	3



**Table 2** Point measurements of crustal thickness (H) and  $V_P/V_S$  ratio from hk-stacking for broadband stations in Saudi Arabia.

Station	PRFs	VP(km/s)	W1	W2	W3	H(km)	$V_P/V_S$	Cor(%)
<b>KACST NETWORK</b>								
<b>affs</b>	88	6.5	0.4	0.3	0.3	36.2±0.4	1.73±0.01	-84.4
<b>arss</b>	22	6.5	0.4	0.3	0.3	38.8±0.4	1.75±0.01	-86.2
<b>ayus</b>	68	6.5	0.4	0.3	0.3	29.3±0.5	1.71±0.02	-86.7
<b>bdas</b>	67	6.5	0.5	0.0	0.5	27.7±0.8	1.75±0.03	-94.3
<b>bljs</b>	104	6.5	0.4	0.3	0.3	38.6±0.3	1.71±0.01	-85.1
<b>djns</b>	86	6.5	0.5	0.5	0.0	42.7±1.1	1.76±0.04	-76.3
<b>haqs</b>	83	6.5	0.5	0.5	0.0	28.2±0.5	1.80±0.04	-82.1
<b>hass</b>	93	6.5	0.5	0.5	0.0	43.7±0.2	1.77±0.01	-85.7
<b>hils</b>	139	6.5	0.4	0.3	0.3	37.1±0.2	1.78±0.01	-76.2
<b>joms</b>	71	6.5	0.5	0.5	0.0	32.0±1.9	1.77±0.05	-98.5
<b>jmqs</b>	41	6.5	0.5	0.5	0.0	38.9±0.9	1.76±0.03	-80.4
<b>kbrs</b>	25	6.5	0.4	0.3	0.3	35.1±0.5	1.74±0.02	-89.4
<b>mzls</b>	87	6.5	0.4	0.3	0.3	41.7±0.8	1.78±0.02	-90.5
<b>nams</b>	62	6.5	0.4	0.3	0.3	41.6±0.4	1.70±0.01	-78.6
<b>qurs</b>	58	6.5	0.4	0.3	0.3	34.2±0.3	1.71±0.01	-68.5
<b>tats</b>	79	6.5	0.4	0.3	0.3	39.7±0.3	1.80±0.01	-89.4
<b>tays</b>	37	6.5	0.4	0.3	0.3	28.7±0.5	1.71±0.02	-90.6
<b>tbks</b>	93	6.5	0.4	0.3	0.3	35.7±0.4	1.76±0.01	-70.4
<b>ynbs</b>	64	6.5	0.4	0.3	0.3	24.8±0.7	1.93±0.05	-88.8

<b>IRIS NETWORK</b>								
<b>afif</b>	53	6.5	0.4	0.3	0.3	36.1±0.3	1.73±0.01	-80.8
<b>halm</b>	74	6.5	0.4	0.3	0.3	36.1±0.3	1.76±0.01	-96.7
<b>rani</b>	30	6.5	0.4	0.3	0.3	37.1±0.8	1.75±0.03	-91.6
<b>rayn</b>	456	6.5	0.4	0.3	0.3	40.2±0.1	1.76±0.00	-86.0
<b>soda</b>	55	6.5	0.4	0.3	0.3	38.2±0.3	1.73±0.01	-88.0
<b>taif</b>	11	6.5	0.4	0.3	0.3	37.2±0.6	1.75±0.03	-91.5
<b>uqsk</b>	31	6.5	0.4	0.3	0.3	36.3±0.4	1.76±0.02	-80.5
<b>SGS NETWORK</b>								
<b>sgs01</b>	30	6.5	0.4	0.3	0.3	39.3±0.7	1.73±0.03	-93.4
<b>sgs02</b>	31	6.5	0.4	0.3	0.3	28.0±0.6	1.73±0.03	-95.6
<b>sgs03</b>	27	6.5	0.4	0.3	0.3	37.1±0.5	1.68±0.02	-95.3
<b>sgs08</b>	12	6.5	0.5	0.5	0.0	39.3±1.6	1.77±0.03	-57.5
<b>sgs09</b>	26	6.5	0.5	0.5	0.0	25.3±0.7	1.81±0.03	-87.0
<b>sgs12</b>	46	6.5	0.5	0.5	0.0	44.9±0.4	1.71±0.01	-84.1
<b>sgs13</b>	43	6.5	0.4	0.3	0.3	45.6±0.7	1.79±0.01	-93.2
<b>sgs16</b>	43	6.5	0.4	0.3	0.3	30.5±0.4	1.79±0.02	-90.4
<b>sgs19</b>	43	6.5	0.4	0.3	0.3	47.7±0.3	1.65±0.01	-55.6
<b>sgs21</b>	7	6.5	0.4	0.3	0.3	35.6±1.7	1.71±0.06	-92.8
<b>sgs22</b>	43	6.5	0.4	0.3	0.3	29.6±0.5	1.69±0.02	-87.50
<b>sgs23</b>	50	6.5	0.4	0.3	0.3	46.2±0.5	1.77±0.01	-84.4
<b>sgs24</b>	59	6.5	0.5	0.5	0.0	47.4±1.3	1.81±0.08	-98.8
<b>sgs25</b>	29	6.5	0.4	0.3	0.3	39.5±1.6	1.75±0.05	-89.4
<b>sgs27</b>	48	6.5	0.4	0.3	0.3	33.1±1.0	1.63±0.04	-86.1

### 3.3 Computation of S-wave receiver functions

The data set for the computation of SRFs consisted of teleseismic S-waveforms for seismic sources located between  $60^\circ$  and  $82^\circ$  epicentral distance and with magnitude  $6.0 m_b$  or larger recorded at broadband seismic stations in Saudi Arabia. At a given station, the converted Sp phase arrives earlier than the direct S phase, and S-to-P conversions upon refraction (Sp) across shallow discontinuities are best observed within the distance range mentioned earlier (Wilson et al. 2006).

To compute the SRFs, the teleseismic S-waveforms were windowed 110 s before and 10 s after the teleseismic S-wave arrival, detrended, and tapered with a cosine taper function of 5% width. The waveforms were then high-pass filtered with a 3-pole Butterworth filter at 20 s to remove long-period noise, and decimated to 10 samples per second after low-pass filtering below 8 Hz to avoid aliasing. Following standard practice in SRF studies (Hansen et al. 2007), the filtered waveforms were rotated into the local ray-coordinate system (LQT system). First, a rotation from the ZNE system into the great-circle path (ZRT system) was performed using the event's back-azimuth. Second, a rotation was performed from the ZRT system into the LQT system, using the method of Sodoudi (2005). In this method, R-Z seismograms for a given event are rotated through a series of incidence angles to create sets of quasi-SV and quasi-P data. Each quasi-SV component is then deconvolved from the corresponding quasi-P component using Ligorria and Ammon (1999) iterative time domain method, with 500 iterations. The optimal incidence angle for rotation into the SH- SV-P coordinate system is the angle that minimizes the direct S-wave energy on the P- component. On the time-reversed receiver functions, the direct S arrival is at 0 s. Therefore, the receiver function of interest is the one which mean amplitude is closest to zero at zero time. The deconvolution was implemented at Gaussian widths of 1.0 ( $f_c \leq 0.5$  Hz) to remove high-frequency noise.

While receiver functions are generated for all events at a given station, it is also important to high-grade the dataset using a number of quality control criteria. Since SRFs tend to be noisier than PRFs, the SRFs are compared to PRFs at the same station to identify the Moho conversion. Only SRFs that display a clear Moho conversion at the appropriate time are used for further analysis. In addition, the amplitude of the Moho conversion can be examined. Using assumed, average velocities for the crust and upper mantle, forward modeling can be used to predict the expected Moho amplitude. If the amplitude of the Moho conversion on the SRF is too large or too small, indicating an unrealistic velocity contrast across the crust-mantle boundary, the SRF is discarded. Generally, the percentage of useable, high-quality data obtained in SRFs analysis is comparable to that obtained in PRF analysis. However, fewer events overall are available for SRFs given the more restricted distance range used, so a large initial dataset is required. Some stations did not include enough data to compute stable SRF averages to be used in the joint inversion.

### 3.4 Lithospheric Thickness

SRFs have stacked and migrated into the depth domain in order to investigate possible occurrences of negative-polarity Sp conversions that may be suggestive of an S-to-P conversion at the base of the lithosphere. The lithosphere-asthenosphere boundary (LAB) is likely to have a thermal origin and therefore be characterized by a gradational transition rather than a sharp discontinuity (Karato, 2003). This may reduce the amplitude of the Sp conversion in the SRFs and make it not identifiable in individual SRF waveforms.

First, phase-moveout curves were computed for each event-station pair for a range of Sp conversion depths ranging between 0 and 300 km at 2 km depth intervals. The phase-moveout curves were obtained after ray tracing through the ak135 global earth model using the TauP utility (Crotwell et al. 1999). Next, the amplitudes for the entire receiver functions were averaged for common Sp conversion depths along the computed phase-moveout curves. Finally, the migrated SRFs were produced by plotting the averaged amplitudes against conversion depth. Confidence bounds were also computed after bootstrapping across the receiver function data set with 200 replications (Efron and Tibshirani, 1991).

Figure (4) displays the SRF stacks for those stations that had individual SRFs with a coherent crustal pattern. Some stations do display small-amplitude Sp conversions at depths that vary between 60 km and 200 km. In general, the stations that are located in the interior of the shield display a negative amplitude Sp conversion under 150 km depth (MZLS, RAYN) or no identifiable Sp conversion at all (AFFS, HILS, QURS), while those stations located along the Red Sea and Gulf of Aqaba (AYUS, BDAS, BLJS, HAQS), and also those near Arabian Gulf (HASS, SGS12, SGS15, SGS19) display negative Sp conversions at shallower depths around 60-80 km.

### 3.5 High-frequency dispersion from ambient- noise cross-correlations

Ambient noise method has been used to image the shear velocity in the crust and uppermost mantle beneath the Arabian Peninsula. We calculated the ambient noise correlation Green's functions for all available station pairs within the Saudi seismic networks, which provide hundreds of characteristic paths exclusively sampling the region. We measured group velocities in conjunction with the joint-inversion of receiver functions and dispersion velocities. Separately, we inverted the Green's function waveforms for the best 1D model along each path and created a 3D model based on those results. Greatest resolution is determined by station density and thus it is greatest along the western part of the kingdom along the Red Sea. The raw data consisted of continuous waveform data for the month of January 2010 from 33 stations in the Saudi national network and an additional 6 stations from stations outside the network.

Following the procedure outlined in Bensen et al. (2007) we cut the data into synchronous hour-long segments, instrument corrected the traces to displacement, removed the mean and the trend and applied a 1% taper. The data were then whitened to equalize the frequency content, and finally converted to single-bit waveforms to minimize the weight of large earthquakes on the correlations (Larose et al. 2004). For each hour, every station was correlated with all the others creating an initial Green's function estimate. This results in a separate correlation waveform for each hour of each day for every pair of stations. By stacking all the hourly correlations, we recover the Green's function with the best signal to noise ratio (SNR). A complete 30-day record would provide us with 720 hours of data; however, incomplete traces reduce this, somewhat. Most of the ambient noise Green's functions in this paper contain more than 660 hours of continuous data with the maximum being 712 hours and the minimum including only 270 hours.

If the source of the coherent noise were uniformly distributed throughout the Earth, the Green's functions would be symmetrical around zero time. Energy traveling from station A to station B would appear at positive time and is often referred to as "causal" energy. Energy traveling from station B to station A would appear at negative time and referred to as "a causal". Ambient noise is known to be in homogeneously distributed and furthermore, seasonal in its occurrence, so the correlations will typically be dominant on either the causal

or a causal side. Additionally the source of the ambient noise varies with frequency, so that the waveform will appear to be dominated by causal energy in some bands and by acausal energy in others. In this study, we take every correlation trace, reverse it around zero time and stack it with the unreversed original. This combines the "causal" ( $t > 0$ ) and "acausal" ( $t < 0$ ) portions of the empirical Green's function. This step results in Green's functions that look symmetric around zero and allows us to perform all of our measurements on the causal trace. Excluding autocorrelations, we obtained Green's function estimates for 528 paths between stations within the Saudi network and 741 paths in total. Separation between stations ranged between 23 km and 3917 km.

## **4. Results and Interpretation**

### **4.1 1D Model Inversions**

The correlation Green's functions have been used as data to invert for shear velocity using a partitioned waveform inversion scheme (Nolet, 1990). The task is to obtain the best 1D model along each path and then merge the paths together to create a 3D image. The optimization was defined to maximize the fit of a synthetic seismogram to the envelope of the Green's function. We used a very-fast simulated annealing technique (Sen and Stoffa, 1995) to search efficiently through model space. Synthetics were created using the reflectivity method described by Randall (1994), which allows rapid calculation of seismograms for 1D-earth models. This allowed us to conduct several thousand iterations and to obtain a separate best fitting model for each of the 741 paths.

Because SNR is a function of distance and frequency, we ran two separate inversion runs: One for data filtered over frequency band between 0.05-0.25 Hz to optimize the strong signal from the short-range data and the other for a frequency band between 0.03-0.09 Hz to avoid the high noise content of the long-range correlations. All models for distances less than 500 km are the result of the 0.05-0.25 Hz run. All models for distances greater than 1100 km are the result of the 0.03-0.09 Hz run.

### **4.2 Localized 3D tomography**

The best fitting 1D models were merged into a 3D model of the subsurface using a partitioned waveform inversion technique (Nolet, 1990). Given the SNR quality of the long-range data, together with the differences in resolution due to station distribution, we focused on the most well resolved region, surrounding the densely instrumented western Kingdom. A grid restricted between  $15^{\circ}$  -  $30^{\circ}$  latitude and  $34^{\circ}$  -  $44^{\circ}$  with a node spacing of  $0.2^{\circ}$ . We also only used the paths for stations separated by less than 1150 km. Based on the data quality issues mentioned above, the result (Fig. 5) should be considered preliminary, and will be enhanced by the joint inversion model. However, it illustrates the large degree of lateral heterogeneity that can be resolved using seismic interferometry in a densely instrumented region.

### **4.3 Joint Inversion Models for the Arabian Shield**

The PRFs jointly inverted and SRFs obtained in task 1 with dispersion velocities measured on the Green's functions obtained in task 2 and with fundamental-mode, Rayleigh-wave, group and phase velocities borrowed from the tomographic studies of Pasyanos (2005)

and Ekström et al. (1997). Using the receiver functions and dispersion measurements, we produced joint inversion models for the broadband stations in Saudi Arabia.

Velocity models from the joint inversion of PRFs, SRFs, and dispersion velocities have been produced for 17 stations in Saudi Arabia, corresponding to stations for which stable SRF estimates could be obtained (Fig. 6). As explained earlier, stable SRF averages are harder to obtain than stable PRF averages due to the reduced epicentral distance range for teleseismic S-wave sources and also due to the fact that Sp conversions occur within the coda of the teleseismic P-wave. Before the inversion, PRFs and SRFs waveforms for each station were sorted by ray parameter and binned within ranges of 0.10 s/km and the receiver functions within each bin were averaged, if the bin included a minimum of three waveforms, to improve the signal-to-noise ratio. Binning around ray parameter values (or, equivalently, incidence angle) before averaging the PRFs and SRFs is important to prevent incoherent overlap of P-to-S and S-to-P conversions, respectively, due to different phase move-outs.

Surface-wave dispersion velocities for the joint inversion were obtained from the independent surface-wave tomography study of Pasyanos (2005). The study measured quality fundamental-mode group velocities along 30,000 Rayleigh wave and 20,000 Love wave paths for periods between 7 and 100 s, and reported lateral variation in group-velocity across Eurasia and North Africa. Although the results of the tomographic study were reported in  $1^\circ \times 1^\circ$  cells, the checkerboard tests showed that the average resolution of the study is around  $4^\circ \times 4^\circ$  (for 50s periods Rayleigh-waves). We identified the tomographic cell containing the selected stations in the Arabian Peninsula and extracted the corresponding dispersion curve, which was then regarded as the local dispersion estimate for that station. As the resolution of the Love waves is poorer than that of the Rayleigh waves (due to fewer measurements and poorer signal-to-noise ratios), we only utilized the Rayleigh-wave dispersion curve.

For the inversions, we considered a starting model consisting of a 40 km-thick crust with a gradational increase between 6.0 and 7.0 km/s in P-wave velocity and a uniform crustal  $V_p/V_s$  ratio of 1.75, overlying a flattened PREM model (Dziewonski and Anderson, 1980). We found a uniform  $V_p/V_s$  ratio justified for the Arabian crust, as values obtained from the hk-stacking analysis do not deviate significantly from this average, in general (see Table 2); for the lithospheric and sub-lithospheric mantle a PREM-like, depth-dependent  $V_p/V_s$  value was assumed. The model was parameterized down to  $\sim 500$  km depth as a stack of thin layers with variable thicknesses of 1.0 km between 0 and 5 km depth, 2.5 km between 5 and 60 km depth, 5 km between 60 and 200 km depth, and 10 km below. We inverted for S-wave velocity structure down to  $\sim 250$  km depth and constrained the structure below that depth to be PREM-like in order to more real display of the partial sensitivity of the long-period surface-waves by wider upper mantle. Joint inversion models were obtained after 6 iterations, using an influence factor  $p=0.5$  and a smoothing of  $\sigma=0.2$ . To equalize the datasets, values for the weights  $w_b$  and  $w_s$  (eq. 4) were obtained by multiplying the number of data points with average data variances of  $\sigma_b^2=5 \cdot 10^{-4} \text{ s}^{-2}$  and  $\sigma_s^2=10^{-4} \text{ km}^2/\text{s}^2$  for the dispersion velocities and receiver functions, respectively.

A detailed joint inversion of PRFs, SRFs, and dispersion velocities is shown in Fig. 6 for station AYUS, located near the Gulf of Aqaba. The velocity model consists of a  $\sim 28$  km thick crust with crustal S-velocities well under 4.0 km/s that increase with depth (the low velocity zone in the uppermost crust is probably not well resolved due to the lack of short-period measurements in the dispersion velocity curve). The crust overlies a pretty thin ( $\sim 15$  km) and slow ( $\sim 4.3$  km/s) upper mantle lid which, in turn, overlies the top of a low-velocity zone with

a minimum velocity around 4.0 km/s at ~60 km depth. The bottom of the low-velocity zone returns to PREM-like velocities at around 180 km depth. The predictions from this model display an excellent agreement with observed PRFs, SRFs and fundamental-mode, Rayleigh-wave, group-velocities.

A summary of all velocity models obtained at the seismic stations in Saudi Arabia is given in Fig. 7. The figure displays the joint inversion models down to 350 km depth (note the bottom 100 km is constrained to be PREM-like) along with stacked PRF and SRF waveforms migrated to depth. In general, the Moho is consistently seen in both PRF and SRF waveforms and as expected, accurately located in the joint inversion models. The lithosphere-asthenosphere boundary (LAB) and the bottom of the low-velocity channel, on the other hand, correspond to smaller velocity contrasts in the velocity models and are therefore harder to see in PRFs. For those discontinuities, the information from the SRFs is critical and has helped constrained lithospheric and sub-lithospheric structure accurately.

Geologically, we would suggest that low velocity beneath the Gulf of Aqaba and southern Arabian Shield and Red Sea at depths below 200 km are related to mantle upwelling and seafloor spreading. Low velocities beneath the northern Arabian Shield below 200 km may be related to volcanism. The low velocity feature near the eastern edge of the Arabian Shield and western edge of the Arabian Platform could be related to mantle flow effects near the interface of lithosphere of different thickness. Additionally, the low-velocity region directly under the Shield can be attributed also to a 115–330 K thermal anomaly in the upper mantle, and this anomaly can be associated with the Cenozoic uplift of and volcanic centers on the Shield.

New results for the lithosphere suggest that the mantle lithosphere is thin and the low velocity zone (LVZ) is significant near the Red Sea, where rifting is active. The mantle lid thickens away from the Red Sea in the Arabian interior. The upper mantle beneath the western portion of the Arabian Shield is anomalously slow, with velocities increasing towards the continental interior. These observations are attributed to thermal differences beneath Saudi Arabia and indicate much hotter mantle beneath the Red Sea than beneath the interior of the shield, which is consistent with plume flow directed beneath the rift.

Generally, the resulting lithospheric structures indicate that the Arabian Platform has an average crustal thickness of 42 km, with relatively low crustal velocities without a strong velocity gradient. The Moho is shallower (36 km) and crustal velocities are 6 per cent higher (with a velocity increase with depth) for the Arabian Shield. Fast crustal velocities of the Arabian Shield result from a predominantly mafic composition in the lower crust. This is consistent with the island arc origin of the westernmost terranes of the Arabian Shield. Lower velocities in the Arabian Platform crust indicate a bulk felsic composition, consistent with orogenesis of this former active margin. The lower mantle velocities and higher Poisson's ratio beneath the Arabian Shield probably arise from a partially molten mantle associated with Red Sea spreading and continental volcanism.

## 5. Conclusions

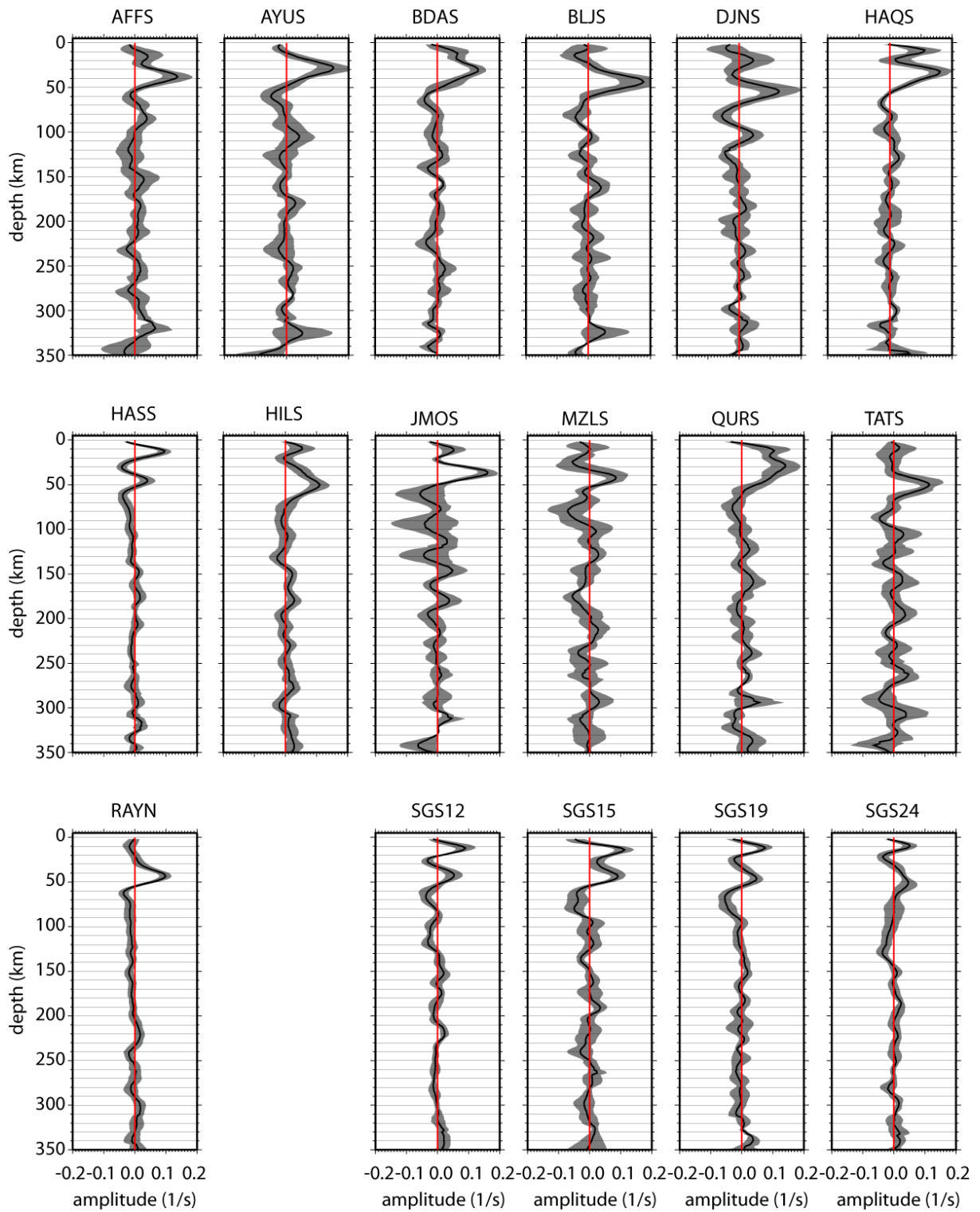
Lithospheric and sub-lithospheric velocity models for 17 broadband stations in Saudi Arabia from the joint inversion of PRFs, SRFs, and Rayleigh-wave group-velocities (fundamental mode) have been developed. The velocity models successfully image detailed S-velocity variation with depth down to ~250 km depth, giving important constraints on key structural parameters such as crustal thickness, lithospheric thickness, lid velocity and (in some instances) thickness and minimum velocity of the low-velocity channel (asthenosphere). Models of crustal and uppermost mantle velocity for the Arabian Shield had been developed in the past from the joint inversion of PRFs and Rayleigh-wave group velocities. The novelty of the velocity models developed under this paper has consisted in the addition of SRF data to extend the velocity models down to lithospheric and sub-lithospheric depths.

It is perhaps a bit disappointing that, out of 50 stations considered, joint inversion velocity models have been developed for just 17 of them. The reason for this low number of selected stations has to be explained in the computation of stable SRF waveforms. Computation of stable SRF waveform averages requires a data set significantly larger than that required for computing stable PRF waveform averages.

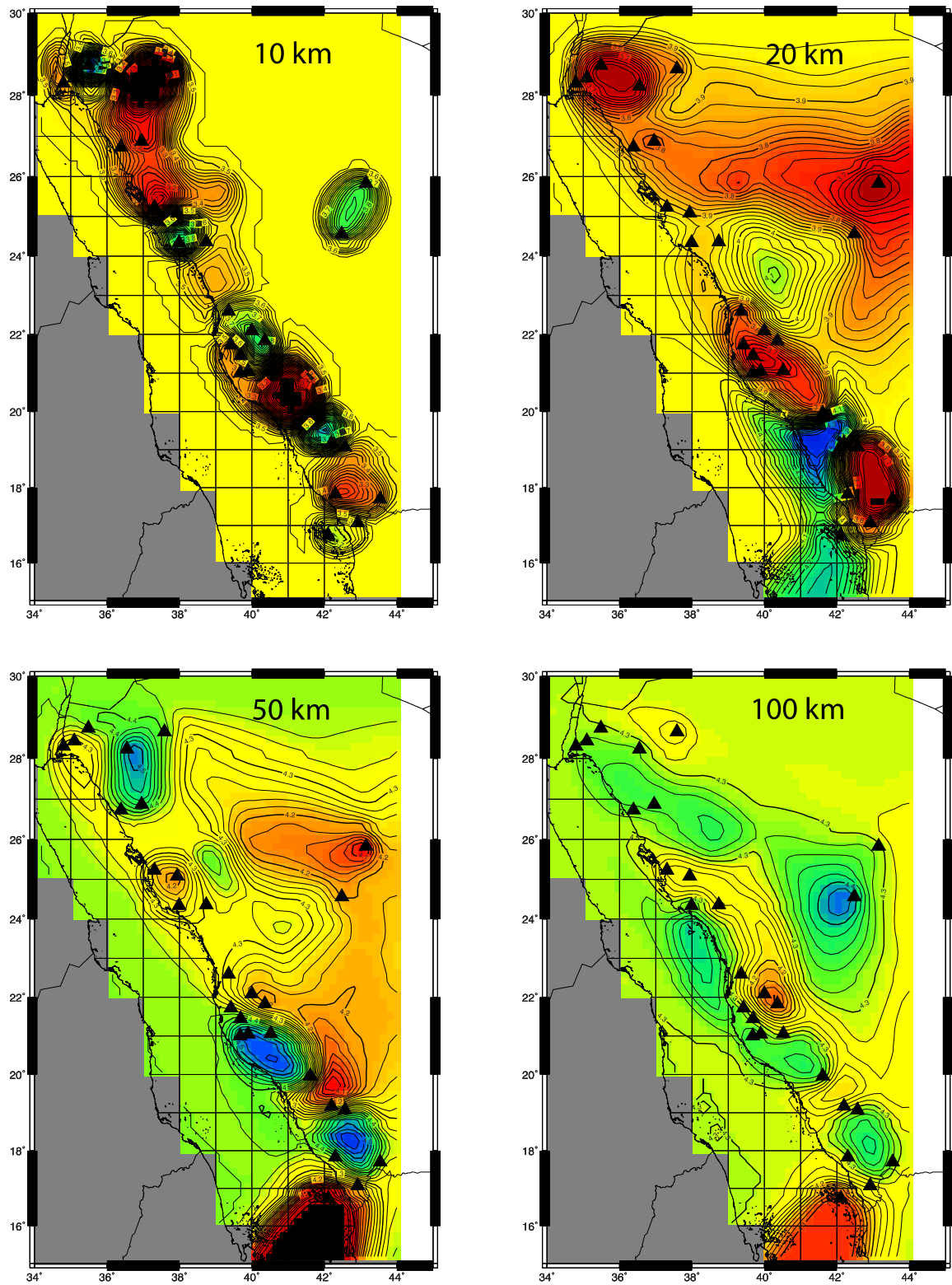
In summary, the 17 S-velocity models have been developed from the joint inversion of PRFs, SRFs and surface-wave (ballistic) dispersion velocities. These models will help better constrain the deep crustal, lithospheric, and sub-lithospheric structure under Saudi Arabia and, in turn, help further our understanding of regional wave propagation in tectonic evolution of the Arabian shield and platform in general.

## Acknowledgments

I would like to express my thanks and gratitude to King Abdulaziz City for Science and Technology for funding the research project AR-30-36. Drs. Jordi Julia and Eric Matzel, as project consultants, whose expert guidance and continuing advice made this work possible. Their willingness to devote their time greatly facilitated the completion of the project I owe them a deep debt of gratitude. I would like also to extend my sincerest thanks to Dr. Michael Pasyanos who helped in performing surface wave group velocity measurements and tomography.

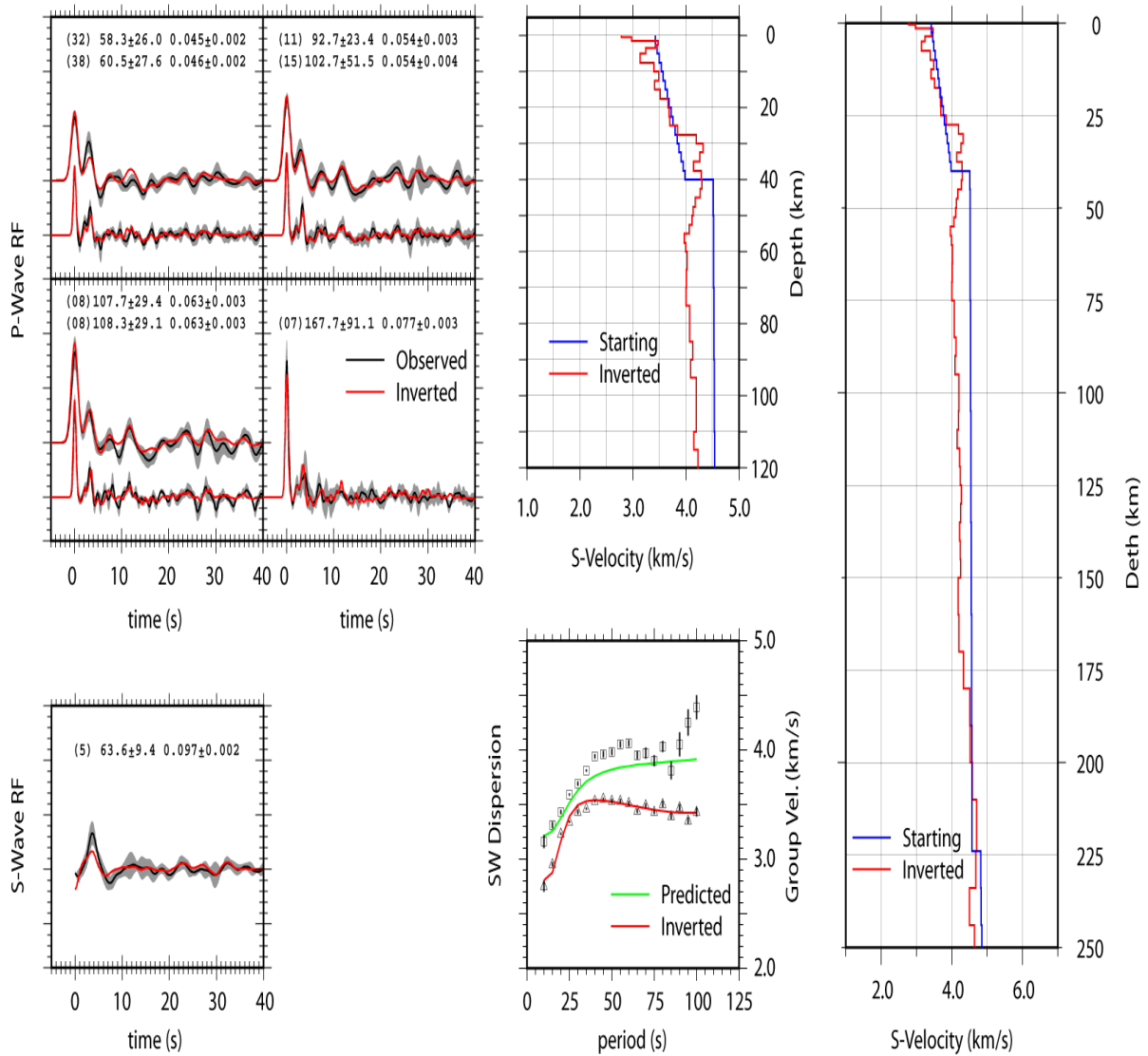


**Fig. 4.** Migrated SRF stacks for several stations in Saudi Arabia. The grey bands are bootstrapped 1s-confidence bounds. Note the clear  $S_p$  conversions at the Moho and the more subtle negative  $S_p$  amplitudes at lithospheric depths.

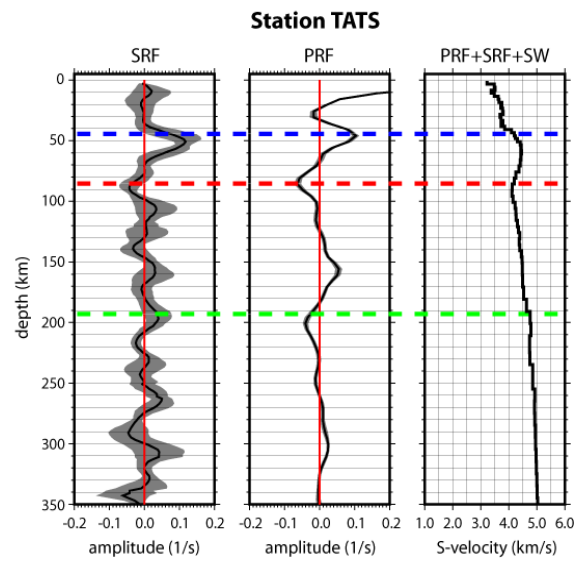
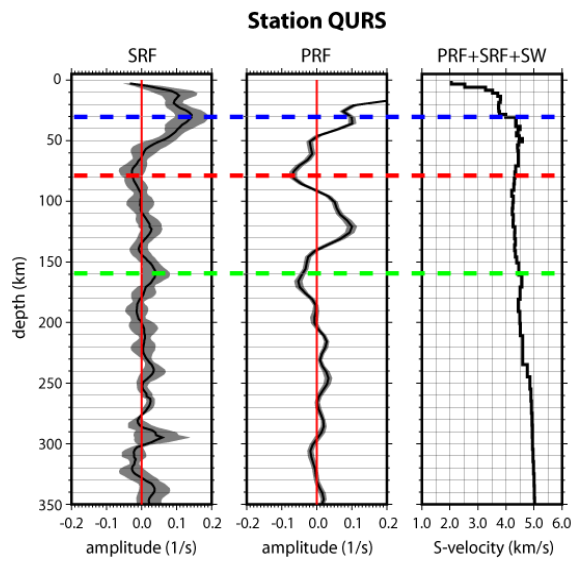
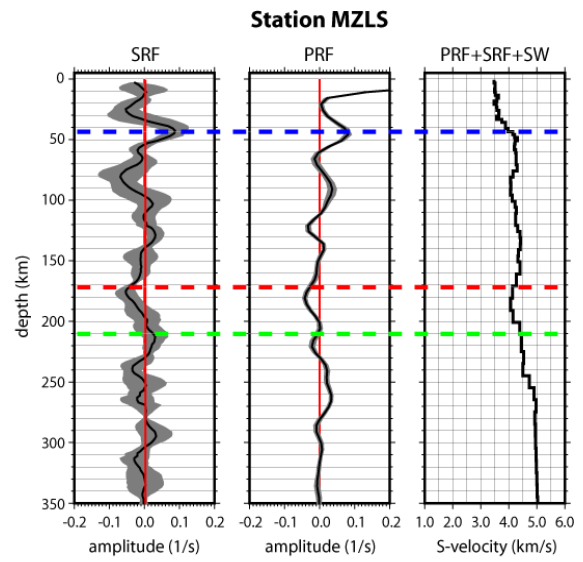
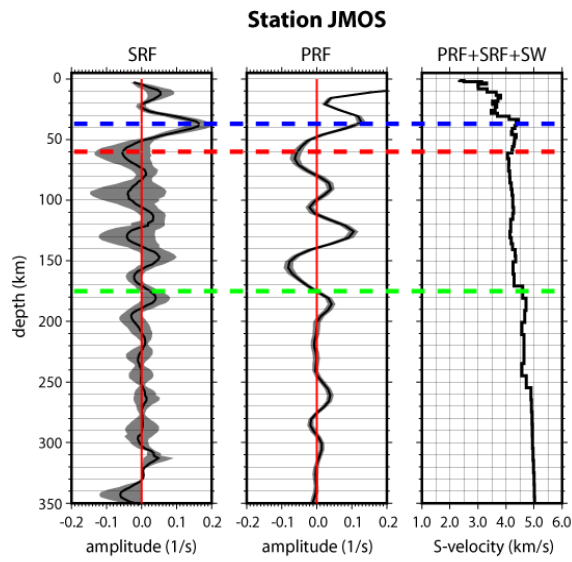
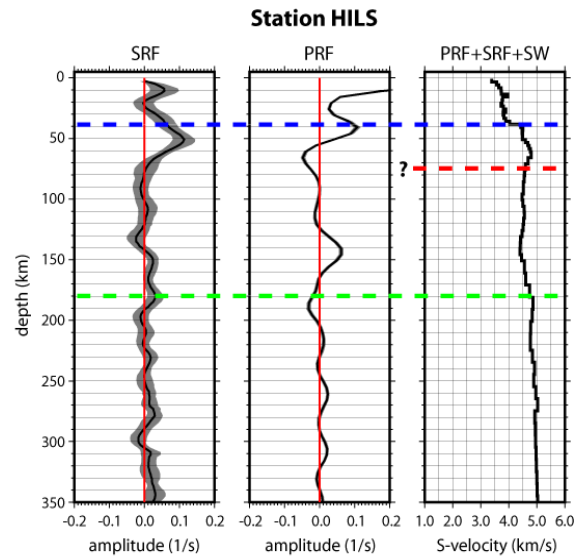
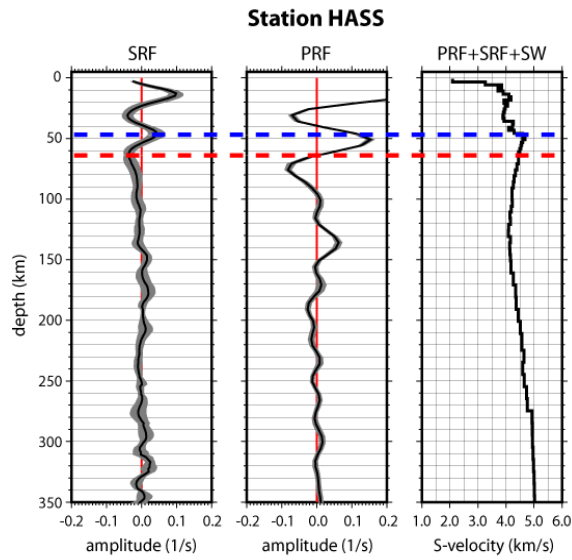


**Fig. 5.** Slices through a localized 3D model at 10, 20, 50 and 100 km.

STATION AYUS - influence = 0.5 smoothness = 0.2-0.4



**Fig. 6.** Joint inversion of PRFs, SRFs, and SW dispersion velocities at station AYUS. The left panels display observed (black) and predicted (red) receiver functions and the middle panel at the bottom displays observed (symbols) and predicted (lines) group velocities. Only fundamental-mode, Rayleigh waves were used during the inversion (red) but a prediction for the fundamental-mode, Love-wave, group velocity is shown (green). The inverted S-velocity model is shown to the right, with the crustal portion enlarged in the middle (top) panel.



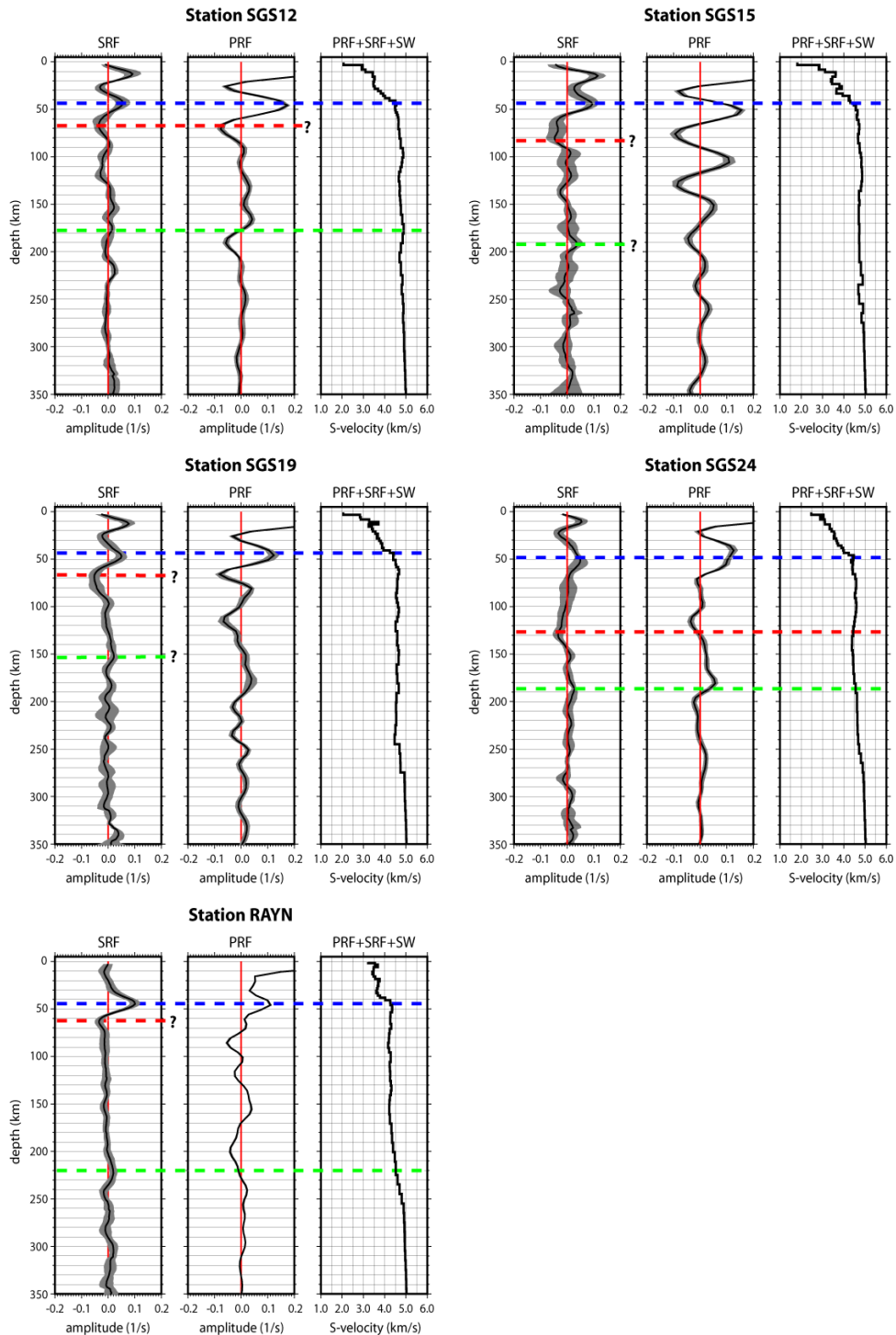


**Fig. 7.** Summary of joint inversion results for broadband stations in Saudi Arabia. Each panel displays the migrated SRF to the left, the migrated PRFs in the middle, and the joint inversion model (S-velocity) to the right. The grey bands indicate  $2\sigma$ -confidence bounds for the stacks. The colored horizontal lines indicate the location of the Moho (blue), LAB (red), and bottom of the asthenosphere (green).

## References

- Al-Amri, A.M. 1998. The crustal structure of the western Arabian Platform from the spectral analysis of long-period P-wave amplitude ratios, *Tectonophysics*, 290, 271-283.
- Al-Damegh, K., Sandvol, E. and Barazangi, M. 2005. Crustal structure of the Arabian plate: New constraints from the analysis of teleseismic receiver functions, *Earth and Planetary Science Letter*, 231, 177-196.
- Bensen, G.D., Ritzwoller, M.H., Barmin, M.P., Levshin, A.L., Lin, F., Moschetti, M.P., Shapiro, N.M. and Yang, Y. 2007. Processing seismic ambient noise data to obtain reliable broadband surface wave dispersion measurements, *Geophys. J. Int.*, 169, 1239–1260.
- Camp, V.E. and Roobol, M.J. 1992. Upwelling asthenosphere beneath western Arabia and its regional implications, *J. Geophys. Res.*, 97, 15255-15271.
- Cassidy, J. 1992. Numerical experiments in broadband receiver function analysis, *Bull. Seis. Soc. Am.*, 82, 1453-1474.
- Crotwell, H.P., Owens, T.J. and Ritsema, J. 1999. The TauP Toolkit: Flexible seismic travel-time and ray-path utilities, *Seism. Res. Lett.* 70, 154-160.
- Debayle, E., Leveque, J. and Cara, M. 2001. Seismic evidence for a deeply rooted low-velocity anomaly in the upper mantle beneath the northeastern Afro/Arabian continent. *Earth Planet. Sci. Lett.* 193, 423-436.
- Dugda, M.T., Nyblade, A.A. and Julià, J. 2007. Thin Lithosphere Beneath the Ethiopian Plateau Revealed by a Joint Inversion of Rayleigh Wave Group Velocities and Receiver Functions, *J. Geophys. Res.*, 112, B08308, doi:10.1029/2006JB004918.
- Durrheim, R. and Mooney W. 1991. Archean and Proterozoic crustal evolution: Evidence from crustal Seismology, *Geology*, 19, 606-609.
- Dziewonski, A. and Anderson, D. 1980. Preliminary reference earth model, *Phys. Earth Planet. Int.*, 25, 297-356.
- Efron, B. and Tibshirani, R. 1991. Statistical data analysis in the computer age. *Science* 253, 390-395.
- Ekström, G., Tromp, J. and Larson, E. 1997. Measurements and global models of surface wave propagation, *J. Geophys. Res.*, 102, 8137-8157.
- Hansen, S., Rodgers, A., Schwartz, S. and Al-Amri, A. 2007. Imaging Ruptured lithosphere beneath the A. Red Sea and Arabian Peninsula, *Earth Planet. Sci. Lett.*, 259, 256-265
- Julià, J., Ammon, C.J. and Herrmann, R.B. 2003. Lithospheric structure of the Arabian shield from the joint inversion of receiver functions and surface-wave group velocities, *Tectonophysics*, 371, 1-21.
- Julià, J., Assumpção, M. and Rocha, M. P. 2008. Deep crustal structure of the Paraná Basin from receiver functions and Rayleigh-wave dispersion: Evidence for a fragmented cratonic root, *J. Geophys. Res.*, 113, B08318, doi:10.1029/2007JB005374.
- Julià, J., Jagadeesh, S., Rai, S.S. and Owens, T.J. 2009. Deep crustal structure of the Indian shield from joint inversion of P wave receiver functions and Rayleigh wave group velocities: Implications for Precambrian crustal evolution, *J. Geophys. Res.*, 114, B10313, doi:10.1029/2007JB006261.
- Julià, J., Ammon, C.J. and Nyblade, A.A. 2005. Evidence for mafic lower crust in Tanzania, East Africa, from joint inversion of receiver functions and Rayleigh wave dispersion velocities, *Geophys. J. Int.*, 162, 555-569.
- Karato, S.I. 2003. The Dynamic Structure of the Deep Earth. An Interdisciplinary Approach, Princeton University Press, 241 pp.

- Keranen, K.M., Klemperer, S.L., Julià, J., Lawrence, J.F. and Nyblade, A.A. 2009. Low lower crustal velocity across Ethiopia: Is the Main Ethiopian Rift a narrow rift in a hot craton?, *Geochem. Geophys. Geosyst.*, 10, Q0AB01, doi:10.1029/2008GC002293.
- Kgaswane, E., Nyblade, A.A., Julià, J., Dirks, P., Durrheim, R.J. and Pasyanos, M. 2009. Shear wave velocity structure of the lower crust in southern Africa: Evidence for compositional heterogeneity within Archaean and Proterozoic terrains, *J. Geophys. Res.*, 114, B12304, doi:10.1029/2008JB00621.
- Langston, C.A. 1979. Structure under Mount Rainier, Washington, inferred from teleseismic body waves, *J. Geophys. Res.*, 84, 4749-4762
- Larose, E., Derode, A., Campillo, M. and Fink, M. 2004. Imaging from one-bit correlations of wideband diffuse wavefields: *Journal of Applied Physics*, 95, 8393–8399.
- Levin, V. and Park, J. 1997. P-SH conversions in a flat-layered medium with anisotropy of arbitrary orientation, *Geophys. J. Int.*, 131, 253-266.
- Ligorria, J.P. and Ammon, C.J. 1999. Poisson's ratio variations of the crust beneath North America, *Seism. Res. Lett.*, 70, 274.
- Lin, F., Moschetti, M.P. and Ritzwoller, M.H. 2008. Surface wave tomography of the western United States from ambient seismic noise: Rayleigh and Love wave phase velocity maps, *Geophys. J. Int.*
- Matzel, E. 2008. Attenuation tomography using ambient noise correlation, *Seismological Research Letters*, 79 (2), 358
- Mooney, M., Gettings, H., Blank, J. and Healy, H. 1985. Saudi Arabian seismic refraction profile: A traveltime interpretation of crustal and upper mantle structure. *Tectonophysics* 111, 173-246.
- Moschetti, M.P., Ritzwoller, M. H. and Shapiro, N. M. 2007. Surface wave tomography of the western United States from ambient seismic noise: Rayleigh wave group velocity maps, *Geochem., Geophys., Geosys.*, 8, Q08010.
- Nolet, G. 1990. Partitioned waveform inversion and two-dimensional structure under the network of autonomously recording seismographs, *J. Geophys. Res.*, 95(B6), 8499–8512.
- Pasyanos, M.E. 2005. A variable resolution surface wave dispersion study of Eurasia, North Africa, and surrounding regions, *J. Geophys. Res.*, 110, doi: 10.1029/2005JB003749.
- Pasyanos, M.E., Walter, W.R. and Matzel, E.M. 2009b. A simultaneous multi-phase approach to determine P-wave and S-wave attenuation of the crust and upper mantle, *Bull. Seism. Soc. Amer.*, 99-6, DOI: 10.1785/0120090061
- Prieto, G.A. and Beroza, G.C. 2008. Earthquake ground motion prediction using the ambient seismic field, *Geophysical Research Letters*, 35, L14304.
- Sen, M. and Stoffa, P.L. 1995. Global optimization methods in geophysical inversion, Elsevier.
- Randall, G.E. 1994. Efficient calculation of complete differential seismograms for laterally homogeneous earth models, *Geophys. J. Int.*, 118, 245-254.
- Shapiro, N.M., Campillo, M., Stehly, L. and Ritzwoller, M.H. 2005. High- Resolution surface wave tomography from ambient seismic noise, *Science*, 307, 1615-1618
- Soudoudi, F. 2005. Lithospheric structure of the Aegean obtained from P and S receiver functions, PhD Thesis, Freie Universität Berlin.
- Stoeser, D. and Camp, V. 1985. Pan-African microplate accretion of the Arabian Shield, *Geological Society of America Bulletin*, 96, 817-826.

- Tkalcic, H., Pasyanos, M., Rodgers, A., Gok, R., Walter, W. and Al-Amri, A. 2006. A multi-step approach in joint modeling of surface wave dispersion and teleseismic receiver functions: Implications for lithospheric structure of the Arabian Peninsula. *J. Geophys. Res.*, 111, doi: 10.1029/2005 JB 004130.
- Wilson, D., Angus, D., Ni, J. and Grand, S. 2006. Constraints on the interpretation of S-to-P receiver functions, *Geophys. J. Int.*, 165, 969–980.
- Zhu, H. and Kanamori, H. 2000. Moho depth variation in southern California from teleseismic receiver functions, *J. Geophys. Res.*, 105, 2969-2980.